Defect States in Compressible Active Polar Fluids with Renewal

Ludovic Dumoulin,[1,2] Carles Blanch-Mercader,[3,*] and Karsten Kruse[1,2,†]
[1]*Department of Biochemistry, University of Geneva, 1211 Geneva, Switzerland*
[2]*Department of Theoretical Physics, University of Geneva, 1211 Geneva, Switzerland*
[3]*Physico-Chimie Curie, Curie Institute, PSL University, 75005 Paris, France*

(Received 9 June 2025; accepted 14 September 2026; published 3 November 2026)

Biological active matter like the cytoskeleton or tissues is characterized by its ability to transform chemical energy into mechanical stress. In addition, it often exhibits orientational order, which is essential for many cellular and morphogenetic processes. Experimental evidence suggests that defects in the orientational order field play an important role in organizing active stress. However, defects tend to annihilate unless the material is in a chaotic state or hydrodynamic interactions are suppressed. Using a hydrodynamic description of compressible active polar fluids, we show that renewal readily leads to a stabilization of defects. Depending on the renewal rate, topological defects arrange in a multitude of different phases, including lattices, active foams, and vortex glasses. Our work suggests that renewal plays a crucial role for organizing biological active matter.

DOI: 10.1103/bnx5-sryc

I. INTRODUCTION

The physics of active matter [1] is known to play a key role in various morphogenetic processes that occur in single cells or tissues. Well-known examples include the formation of lamellipodia in migrating single cells [2], apical constriction during gastrulation of the fruit fly *Drosophila melanogaster* [3], or cortical actin flows during head-tail symmetry breaking in the nematode *Caenorhabditis elegans* [4]. These processes are driven by gradients in active stress, which is generated autonomously by the biological systems through the conversion of chemical energy released during the hydrolysis of adenosine-triphosphate (ATP) into mechanical work. How gradients in active stress are organized to result in the observed morphogenetic events remains largely unknown.

On a molecular level, active stress is generated by motor proteins that interact with protein filaments, for example, myosin motors and actin filaments. The stress generated in this way is anisotropic due to the elongated form of the filaments. This molecular anisotropy can translate to macroscopic orientational order when filaments align on cellular scales or when elongated cells align on tissue scales. The corresponding orientational order fields are often nematic [5,6], when the arrangement is invariant under inversion of the orientation, or polar [7–9], when this invariance is broken. Higher order orientational order is also possible [10]. Active stress is tightly coupled to the orientational order in a cell or tissue [11].

In recent years, experimental evidence has accumulated that topological defects play an important part in organizing active stress [12–15]. These defects are singularities of the orientational field and are characterized by their topological charge [16]. Defects can themselves be oriented [17,18], but the interaction of defects is not fully accounted for by local properties [19]. Topological defects can lead to the accumulation of stress [12,20], which could be related to the localization of cell death [12], accumulation [13] as well as differentiation [15], but also to morphogenetic processes like the formation of protrusions [14,15,21,22].

In passive materials with orientational order, topological defects tend to spontaneously annihilate, unless their existence is required by the boundary conditions or the system's topology through the Poincaré-Hopf theorem. In contrast, active stress can lead to a continuous proliferation of singularities in the orientation field [5,23,24]. However, this proliferation is related to chaotic dynamics—or low Reynolds number turbulence [25]—such that it does not seem to be appropriate for a robust organization of active stress. Mechanisms for stabilizing topological defects in active matter remain largely elusive. Theoretical studies suggest that anisotropic substrates [26] and coupling to extrinsic curvature can generate orientational defect alignment [27]. In turbulent states, defect binding has been reported [28]. Finally, substrate friction leads to stable defect lattices [29–31].

In spite of a large body of theoretical work on the dynamics of defects [32] and the accumulating evidence that topological defects organize active stress during developmental processes [33,34], the effects of renewal on defects in active fluids are hardly known. In this work we introduce generalized hydrodynamic equations for compressible active polar fluids in the presence of renewal [Fig. 1(a)]. We find that renewal can stabilize topological defects. Using

*Contact author: carles.blanch-mercader@curie.fr
†Contact author: karsten.kruse@unige.ch

Published by the American Physical Society under the terms of the Creative Commons Attribution 4.0 International license. Further distribution of this work must maintain attribution to the author(s) and the published article's title, journal citation, and DOI.

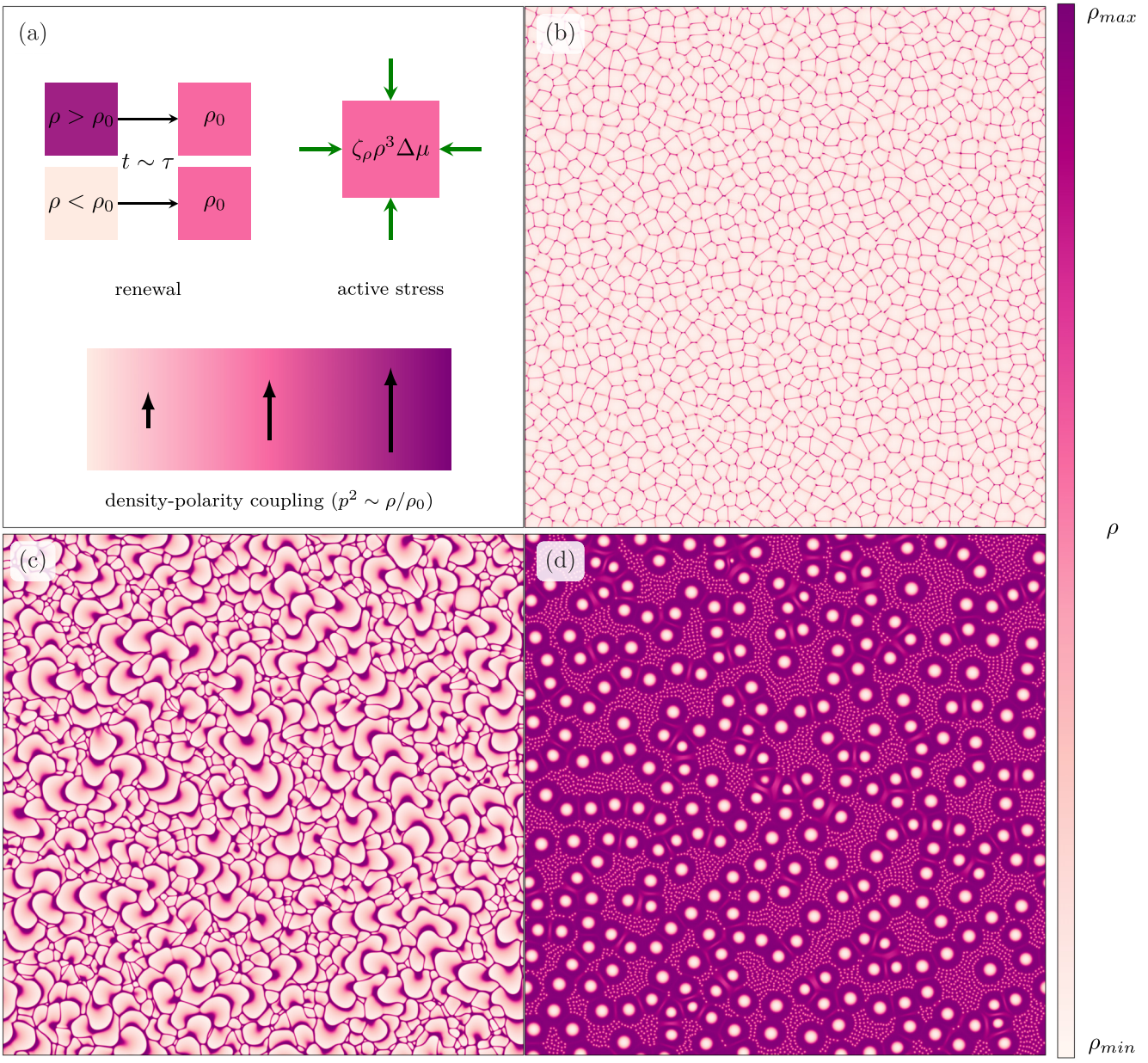


FIG. 1. Compressible active polar fluids in the presence of renewal. (a) Schematic of the physical processes considered in this work: renewal, active stress, and density-polarity coupling. (b)–(d) Snapshots of the density heatmaps from numerical solutions of the dynamic equations presented in Sec. II. Parameters are $\rho_0 = 0.45$ (b), $\rho_0 = 0.6$ (c), and $\rho_0 = 0.75$ (d) as well as $\tau = 5$ and $\zeta_\rho = 4$. In (b)–(d) the system size is $L = 50$. Other parameter values as in Table I. Maximal and minimal densities are, respectively, $\rho_{\max} = 0.96$ and $\rho_{\min} = 0.37$ (b), $\rho_{\max} = 0.87$ and $\rho_{\min} = 0.44$ (c), and $\rho_{\max} = 0.79$ and $\rho_{\min} = 0.58$ (d).

long-time numerical solutions of the dynamic equations in large systems, we find a number of different states, including active foams, density waves, and vortex glass states [Figs. 1(b)–1(d) and Movies S1–S3 [35]]. In the presence of anisotropic active stress additional phases appear. We show that the linear dynamics of density and polarity perturbations rationalize selection of the phases. These results indicate a central role of renewal in stabilizing topological defects and suggest a basic mechanism for a well-controlled organization of active stress.

II. HYDRODYNAMICS OF AN ACTIVE POLAR FLUID IN THE PRESENCE OF RENEWAL

Motivated by the actin cortex, we study a two-component system consisting of a compressible active polar fluid and a passive fluid on a two-dimensional space [36–39], Fig. 1(a). In the context of the actin cortex, the former represents the acto-myosin network and the latter the cytoplasm containing actin monomers and unbound molecular motors. In the following, we derive hydrodynamic equations that describe the system's behavior on large space and time scales. As in Ref. [38], we

neglect permeation flows of the passive component and focus only on the active component from here on. We denote the corresponding mass density by ρ and its velocity field by $\mathbf{v}$. In addition, the active component can exhibit macroscopic polar order, which is captured by the polarity field $\mathbf{p}$.

The equilibrium behavior of the system is determined by the total free energy $\mathcal{F} = \int f d^2\mathbf{r}$, where $d^2\mathbf{r}$ is an infinitesimal area element and f is the free-energy density f given by

$$f = \frac{a}{4}\rho^4 + \rho^2\left(-\frac{\chi}{2}\frac{\rho}{\rho_0}|\boldsymbol{p}|^2 + \frac{\chi}{4}|\boldsymbol{p}|^4 + \frac{\kappa}{2}(\nabla \boldsymbol{p})^2\right). \quad (1)$$

The first term captures the energetic cost for concentrating the active component with an elastic coefficient a. Due to steric interactions between the components of the actomyosin networks and between them and other solutes in the cytoplasm, the maximal active fluid density is limited. We account for this limit by choosing this term to be quartic in the mass density ρ. Note that this choice also suppresses density divergences. As long as it is large enough, the precise value of the exponent is not important though. The remaining terms correspond to the Landau-Ginzburg free energy for the polarity field $\mathbf{p}$ [16]. For $\chi > 0$, we have $|\mathbf{p}|^2 = \rho/\rho_0$ in equilibrium, reflecting an increase of polar order with increasing density. For the time being, ρ_0 is some reference density. The final term penalizes distortions of the polarity field with an elastic constant κ [16]. We neglect a potential spontaneous splay term.

In the presence of polar order, the hydrostatic pressure generalizes to the Ericksen stress σ^{e} with components

$$\sigma^{\mathrm{e}}_{\alpha\beta} = (f - \rho\mu)\delta_{\alpha\beta} - \frac{\partial f}{\partial(\partial_\beta p_\gamma)}\partial_\alpha p_\gamma, \quad (2)$$

where Greek indices run from 1 to 2 and $\delta_{\alpha\beta} = 1$ if $\alpha = \beta$ and zero otherwise. We adopt the convention that summation is implied over repeated indices. In the above expression, $\mu = \frac{\delta\mathcal{F}}{\delta\rho}$ is the active fluid's chemical potential and $h_\alpha = -\frac{\delta\mathcal{F}}{\delta p_\alpha}$ are the components of the molecular field. We give their expressions in Appendix A. The isotropic part of σ^{e} can be interpreted as a pressure, $\Pi^{\mathrm{eff}} = -f + \rho\mu$ with

$$\Pi^{\mathrm{eff}} = \frac{3}{4}a\rho^4 - \rho^2\left(\chi\frac{\rho}{\rho_0}|\mathbf{p}|^2 - \frac{\chi}{4}|\mathbf{p}|^4 - \frac{\kappa}{2}(\nabla \boldsymbol{p})^2\right). \quad (3)$$

In equilibrium, when $|\mathbf{p}|^2 = \rho/\rho_0$, the effective isothermal compressibility $\frac{1}{\rho}\frac{\partial\rho}{\partial\Pi}$ is positive only if $\rho_0 > \sqrt{5\chi/6a}$. For smaller values of ρ_0, the system is thermodynamically unstable.

We now turn to the dynamics of the system. We assume that it is maintained out of equilibrium by the continuous consumption of a chemical fuel. In the case of the actin cortex, this fuel is adenosine triphosphate (ATP), which is hydrolyzed to form adenosine diphosphate (ADP) and inorganic phosphate (P_i). The hydrodynamic description is based on conservation laws for mass and momentum and on the broken continuous symmetry under rotations resulting from the polar field [40].

Mass conservation of the active fluid reads

$$\partial_t\rho + \partial_\alpha(\rho v_\alpha) + \partial_\alpha j_\alpha = -\tau^{-1}(\rho - \rho_0). \quad (4)$$

The total material current is decomposed into an advective part $\rho\mathbf{v}$ and a diffusive part $\mathbf{j}$. The source terms account for assembly and disassembly of the active fluid. We consider a linear expression for renewal, which is determined by the characteristic timescale τ and the target density, which we take to be equal to ρ_0. The values of ρ_0 and τ are related to the fluid's assembly and disassembly rates k_a and k_d via $\tau = k_d^{-1}$ and $\rho_0 = k_a/k_d$. In the context of tissues, these rates are associated with cell division and cell death processes, [41,42]. We take τ and ρ_0 to be constant and indicate in the discussion how heterogeneity of renewal could be captured.

As cytoskeletal flows or tissue flows are typically associated with a low Reynolds number, we neglect inertial effects. From now on, ρ denotes the number density of the active fluid, which is related to its mass density by some molecular mass that we consider to be constant. Furthermore, momentum conservation reduces to the force balance equation

$$\partial_\beta\sigma^{\mathrm{tot}}_{\alpha\beta} = \xi v_\alpha, \quad (5)$$

where σ^{tot} denotes the total stress tensor. The right hand side corresponds to a viscous friction term with friction coefficient ξ. For the actomyosin cortex, it mainly results from interactions between the actomyosin network and the cell membrane or an underlying substrate although permeation of the actomyosin network by the cytosol also contributes to this term.

To close the system of equations, we need to provide constitutive equations of the active fluid. Following the standard approach of nonequilibrium thermodynamics [43], we identify the thermodynamic forces conjugate to the fluxes and express the latter to linear order in terms of the former. Explicitly, the fluxes are the symmetric part of the deviatory stress $\sigma^{\mathrm{d}} \equiv \sigma^{\mathrm{tot},s} - \sigma^{\mathrm{e},s}$, the diffusive current $\mathbf{j}$, the convected corotational derivative of the polar field $\mathrm{D}\mathbf{p}/\mathrm{D}t$, and the rate r of ATP hydrolysis. Here the superscript s denotes the symmetric part of the respective tensors and the convected corotational derivative is defined by $\mathrm{D}p_\alpha/\mathrm{D}t = \partial_t p_\alpha + v_\beta\partial_\beta p_\alpha + \omega_{\alpha\beta}p_\beta$, where $\omega_{\alpha\beta} = (\partial_\alpha v_\beta - \partial_\beta v_\alpha)/2$ are the components of the vorticity tensor. Note that the total stress tensor in Eq. (5) also contains an antisymmetric part such that

$$\sigma^{\mathrm{tot}}_{\alpha\beta} = \sigma^{d}_{\alpha\beta} + \sigma^{\mathrm{e}}_{\alpha\beta} + \tfrac{1}{2}(p_\alpha h_\beta - p_\beta h_\alpha). \quad (6)$$

The conjugated thermodynamic forces are the symmetric part of the velocity gradient tensor with components $v_{\alpha\beta} = (\partial_\alpha v_\beta + \partial_\beta v_\alpha)/2$, the gradient of the active fluid's chemical potential μ, the molecular field $\mathbf{h}$, and the difference in chemical potentials of ATP and its hydrolysis products $\Delta\mu = \mu_{\mathrm{ATP}} - \mu_{\mathrm{ADP}} - \mu_{\mathrm{P}}$. Explicitly, the constitutive equations are

$$\sigma^{\mathrm{d}}_{\alpha\beta} = 2\eta v_{\alpha\beta} + \frac{\nu}{2}(h_\alpha p_\beta + h_\beta p_\alpha) + \rho\Delta\mu(\zeta_\rho\rho^2\delta_{\alpha\beta} + \zeta_p p_\alpha p_\beta), \quad (7)$$

$$j_\alpha = -\gamma\partial_\alpha\mu, \quad (8)$$

$$\mathrm{D}p_\alpha t = -\nu p_\beta v_{\alpha\beta} + \frac{1}{\Gamma}h_\alpha. \quad (9)$$

Here, for simplicity, among others we have neglected a term proportional to $\mathbf{p}$ in Eq. (8) and terms containing gradients of the chemical potential μ in Eqs. (7) and (9). Also, in principle, the distributions of ATP, ADP, and P_i should be treated as dynamic fields. However, we consider $\Delta\mu = \text{const}$ as only

TABLE I. Values of the dimensionless parameters used in this work. Dimensionless parameters are denoted by the same symbol as the corresponding dimensional parameter, with a prime. The relation between dimensionless and dimensional parameters, as well as the choice of unit system, is detailed in Appendix B. * $a' = 4/3$ if $\zeta_\rho = 0$. For simplicity, we omit the prime notation in Secs. III–V.

Parameter	ρ_0'	a'	χ'	κ'	ν'	ζ_ρ'	ζ_p'	γ'	Γ'	τ'	$\Delta\mu$
value	0.4-1.5	$4\zeta_\rho'/3$ *	0.1	10^{-4}	0	0–24	0	10^{-4}	1	0.01–100	1

a few examples of spatiotemporal ATP patterns have been reported so far (for example, [44]).

The constitutive equations contain a number of phenomenological parameters that characterize the material properties. The shear viscosity η, the rotational viscosity Γ, the mobility coefficient γ, and the flow-alignment coefficient ν are familiar from conventional liquid crystals. In addition, there are active coefficients ζ_ρ and ζ_p that couple the deviatoric stress $\sigma^{\rm d}$ to the chemical potential difference $\Delta\mu$. We have neglected a potential coupling between $\Delta\mu$ and the time derivative of the polarization as it amounts to a redefinition of the equilibrium polarization amplitude [45]. In agreement with the Curie principle, we have used the polarization $\mathbf{p}$ to couple fluxes and forces of different tensorial order. Furthermore, we included a dependence on the density ρ in the active terms, because active stress is expected to increase with the active fluid's density. Similar hypotheses have been used in other descriptions of the actomyosin cortex [38,46].

In the following, we use the dynamic equations in nondimensionalized form. Unless stated otherwise, the parameter values given in Table I. The values of τ, ρ_0, and ζ_ρ are varied. Additionally, in Eq. (7) we ignored an isotropic viscous stress $\bar\eta v_{\gamma\gamma}\delta_{\alpha\beta}$, an isotropic active stress $\bar\zeta_p p_\gamma p_\gamma \delta_{\alpha\beta}$, and an isotropic elastic stress $\bar\nu h_\gamma p_\gamma \delta_{\alpha\beta}$, as we checked that our results are robust to variations in the parameters $\bar\zeta_p$ and $\bar\nu$. Finally, we set $\Delta\mu = 1$ to simplify the notation.

III. DEFECT STABILIZATION THROUGH RENEWAL

Through minimization of the free energy associated with orientational order, pairs of topological defects with opposite charges tend to merge and annihilate upon relaxation to thermodynamic equilibrium [17–19]. In the absence of noise, this relaxation process stops, when the defect configuration with minimal energy and consistent with the boundary conditions is reached. In contrast, active processes can promote the separation of defect pairs and even increase their number [5,47]. For active nematics, this requires, for instance, an anisotropic active stress [48]. In polar fluids, we find that renewal can stabilize topological defect pairs both in the presence or absence of active stress (Fig. 2 and Movies S4 and S5 [35]). In this section we show that, in the presence of renewal, topological defects are associated with a continuous matter outflow sustained by renewal. This effect underlies an effective repulsion and thus stabilization of defects.

We consider the rotationally invariant steady-state solution of the dynamic equations presented in the previous section for an aster with $\rho \equiv \rho(r)$, $\mathbf{p} \equiv p(r)\mathbf{e}_r$, and $\mathbf{v} \equiv v(r)\mathbf{e}_r$, where r is the radial coordinate and $\mathbf{e}_r$ the radial unit vector. We focus on the case when active stress and flow alignment are absent, $\Delta\mu = 0$ and $\nu = 0$. Under these conditions, we obtain for the chemical potential μ and the molecular field $\mathbf{h} = h\mathbf{e}_r$

$$\mu = a\rho^3 - \frac{3\chi}{2\rho_0}\rho^2 p^2 + \frac{\chi}{2}\rho p^4 + \kappa\rho\left((\partial_r p)^2 + \frac{p^2}{r^2}\right), \quad (10)$$

$$h = \frac{\chi}{\rho_0}\rho^3 p - \chi\rho^2 p^3 + \kappa\left(\frac{\partial_r(\rho^2 r\partial_r p)}{r} - \frac{\rho^2 p}{r^2}\right). \quad (11)$$

If we denote the radial component of the divergence of the Ericksen stress as $f_r^{\rm e}$, then

$$f_r^{\rm e} = -\rho\partial_r\mu - h\partial_r p, \quad (12)$$

where μ and h are given by Eqs. (10) and (11), respectively.

Finally, the dynamic equations, Eqs. (4), (5), and (9), reduce to

$$\partial_t\rho + \frac{1}{r}\partial_r(r(\rho v - \gamma\partial_r\mu)) = -\tau^{-1}(\rho - \rho_0), \quad (13)$$

$$\xi v - 2\eta\left(\partial_r^2 v + \frac{1}{r}\partial_r v - \frac{1}{r^2}v\right) = f_r^{\rm e}, \quad (14)$$

$$\partial_t p + v\partial_r p = \Gamma h. \quad (15)$$

A numerical solution of the dynamic equations shows that the density is minimal at the defect location $r = 0$ [Fig. 3(a)]. As

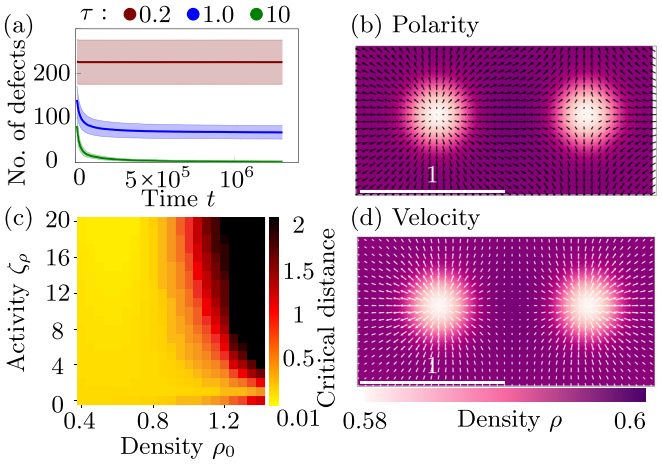


FIG. 2. (a) Number of defects as function of time for different values of τ and $\rho_0 = 1$, $\zeta_\rho = 4$, $L = 10$. Solid lines: number of defects averaged over 50 runs per τ, shaded area: standard deviation. (b) Snapshot of density (heatmap) and polarity (black arrows) maps for a pair of topological defects. Parameters: $\rho_0 = 0.6$, $\tau = 1$, $\zeta_\rho = 12$. The image was cropped from a square domain of length $L = 10$. (c) Critical distance below which a pair of oppositely charged defects annihilates, as a function of ρ_0 and ζ_ρ for $\tau = 1$ and $L = 10$. The black region corresponds to a critical distance larger than half of the system size $L/2$. (d) Snapshot of density (heatmap) and velocity (white arrows) maps for the same defect pair shown in panel (b).

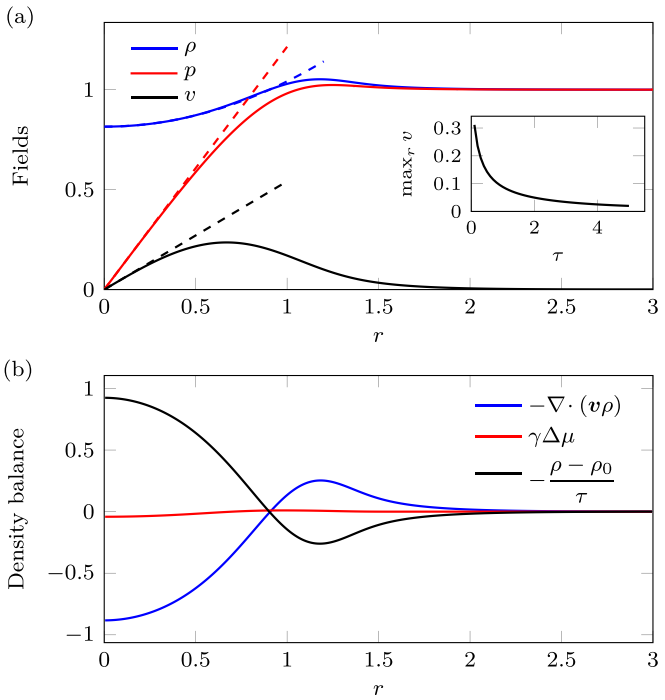


FIG. 3. Steady-state configuration of a single defect at $r = 0$. (a) Numerical solution of Eqs. (13) and (14). Full lines: density ρ (blue), polarization p (red), and velocity v (black). Dashed lines: approximation for small r; see text. Inset: (c) Maximal fluid velocity as a function of the turnover time τ. (b) Spatial dependence of the divergence of the advection flux $v\rho$ (blue), the diffusive flux $-\gamma\,\partial_r\mu$ (red), and renewal $-(\rho-\rho_0)/\tau$ (black). Parameter values are $\chi = 1$, $\gamma = 10^{-2}$, $\tau = 0.2$, $\kappa = 10^{-3}$, $\zeta_\rho = 0$, and as in Table I.

the distance from the defect increases, the density increases and overshoots before relaxing to its target value, ρ_0. Similarly, the polar order increases with the radial distance, reaches a maximum, and then converges to the value $p = 1$, the value that minimizes the Landau-Ginzburg contribution to the free energy (1). This configuration is accompanied by an outward material flow that initially increases with distance from the defect before decaying to zero. In steady state, this advective flux is largely balanced by fluid renewal, whereas diffusion, which results in a flux toward the defect, contributes only weakly [Fig. 3(b)].

For sufficiently small r, we can approximate the steady-state density, polarization, and velocity fields by

$$\rho = \bar{\rho}\left(1 + \frac{r^2}{\lambda_\rho^2}\right), \tag{16}$$

$$p = \frac{r}{\lambda_p} + \frac{r^3}{\bar{\lambda}_p^3}, \tag{17}$$

$$v = \frac{r}{\tau_v}\left(1 + \frac{r^2}{\lambda_v^2}\right). \tag{18}$$

By substituting these expressions into the dynamical equations and matching coefficients of equal powers of r, we obtain relations between the constants $\bar{\rho}$, λ_ρ, λ_p, $\bar{\lambda}_p$, τ_v, and λ_v. Explicitly, we consider the first-order terms in Eqs. (14) and (15), and the zeroth- and second-order terms in Eq. (13). However, in each order, the viscous term and the splay diffusion term proportional to κ introduce dependencies on higher order terms. The profiles are thus not entirely determined by the local dynamics but require information from the system boundary at $r = r_{\max}$, where we impose $\rho(r_{\max}) = \rho_0$ and $p(r_{\max}) = 1$.

As we have chosen $\kappa = 10^{-3}$, it is appropriate to neglect the splay diffusion term. In this case, the condition resulting from Eq. (15) yields

$$\tau_v = \rho_0 \Gamma^{-1} \chi^{-1} \bar{\rho}^{-3}. \tag{19}$$

The slope of the velocity is thus determined by the core density alone. From force balance, Eq. (14), we can express λ_v in terms of $\bar{\rho}$, λ_ρ and λ_p. These three values are linked by the continuity Eq. (13):

$$2\Gamma\chi\bar{\rho}^4 - \frac{12\gamma a\rho_0}{\lambda_\rho^2}\bar{\rho}^3 + \frac{6\gamma\chi}{\lambda_p^2}\bar{\rho}^2 + \frac{\rho_0}{\tau}\bar{\rho} - \frac{\rho_0^2}{\tau} = 0. \tag{20}$$

This leaves two free parameter at the lowest order. We obtain the values of $\bar{\rho}$ and λ_p from the numerical solutions. The values of λ_ρ and τ_v are then determined by Eqs. (19) and (20). The approximate fields agree well with the numerical solutions for sufficiently small values of r [Fig. 3(a)].

If, in the continuity equation, we also neglect the contribution of the diffusion term, which contributes only a little [Fig. 3(a)], then $2\Gamma\chi\bar{\rho}^4 = \frac{\rho_0}{\tau}(\rho_0 - \bar{\rho})$, such that $\bar{\rho}$ is fully determined by material parameters, in particular, τ. For the parameter values this gives $\bar{\rho} \simeq 0.82$, which is close to the value 0.815 of the numerical solution of the full equations.

From the analysis in this section, we conclude that, in the presence of renewal, it is favorable for the fluid density to decrease below its target value at the defect location. Continuous material injection at the defect then generates a net outward flux. The maximum flow velocity increases with decreasing turnover time τ [Fig. 3(a), inset].

In large systems, these flows lead to a sustained finite density of defects. As these flows are eventually driven by material renewal, one might expect that the maximum defect density increases with the renewal rate τ^{-1} [Fig. 3(a), inset]. Indeed, with larger flows, defects can be kept separate at smaller distances in spite of the increased cost of polar field deformations. This is typically the case (Fig. 4). The precise value of the maximal density, however, depends on the full radial velocity profile and not just its maximum. In addition to the turnover rate τ^{-1}, it also depends on the target density ρ_0. The target density enters the dynamic equations through the renewal term in Eq. (4). For an increase of ρ_0, one might expect an increase of renewal, hence, of the flux and of effective defect repulsion, which should lead to a decrease of the final defect density. This is indeed what we observe (Fig. 4).

The picture changes, when active stress is included. Indeed, the parameter ζ_ρ affects the critical distance at which two defects annihilate [Fig. 2(c)], which in turn dictates the final defect density (Fig. 4). Generally, an increase in ζ_ρ leads to a decrease in the defect density. Furthermore, it can render the dependence of the defect density on the target fluid density ρ_0 nonmonotonic. We provide more insight into this dependence

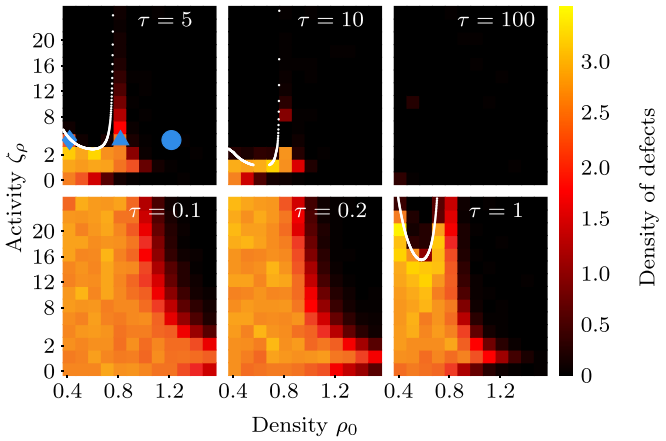


FIG. 4. Defect density in the (ρ_0, ζ_ρ) plane for different values of τ. For each data point, a single numerical solution for a system size of $L = 10$ has been analyzed. White dots indicate the critical activity ζ_ρ^c obtained by solving Eq. (23) with $a = 4\zeta_\rho^c/3$ (values of $\zeta_\rho^c < 1$ are not shown). Blue symbols indicate solutions for $\rho_0 = 0.4$ (diamond), 0.8 (triangle), and 1.2 (circle) shown in Fig. 6 below. Other parameter values as in Table I.

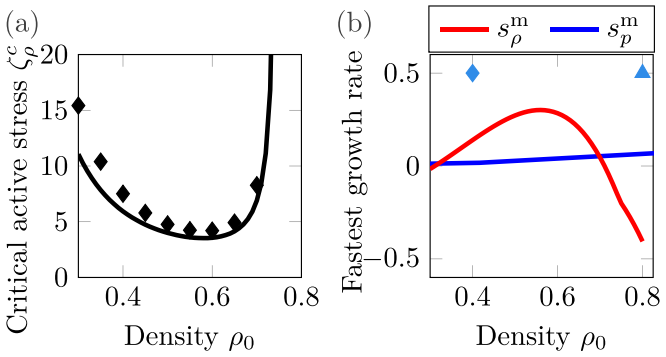


FIG. 5. Linear stability analysis of homogeneous states. (a) Stability diagram of the homogeneous polar stationary state as a function of ρ_0 and ζ_ρ for $\tau = 5$ and $a = 4/3\zeta_\rho^c$. Solid line: density and polarity perturbations; diamonds: only density perturbations. (b) Fastest growth rate of density (red) and polarity (blue) perturbations of the homogeneous isotropic state for $\zeta_\rho = 4$ and $\tau = 5$, other parameters as in Table I. Diamond and triangle indicate the same parameter values as in Fig. 4.

through a linear stability analysis, which we present in the following section.

IV. DEFECT STATES FOR ISOTROPIC ACTIVE STRESS

In this section we show how topological defects arrange as a function of the target density ρ_0, which is set by the renewal rates. We start with a linear stability analysis of the homogeneous polarized state. Then we present numerical solutions of the dynamic equations, and finally rationalize the observed sequence of states using a linear stability analysis of the isotropic state.

A. Linear stability analysis

Consider the uniform polarized state, $\rho = \rho_0$ and $\mathbf{p} = \mathbf{p}_0$ with $|\mathbf{p}_0|^2 = 1$, which is a steady state of the dynamic equations (1)–(9). The linearized dynamics for a small perturbation of this state is given in Appendix C. The ensuing stability diagram shows that this state is unstable for a critical level of active stresses $\zeta_\rho > \zeta_\rho^c$, where the critical value ζ_ρ^c is a nonmonotonic function of the target density ρ_0 [Fig. 5(a)].

The instability is mainly driven by fluctuations in the density. To see this, we computed the growth rate s_ρ associated with density fluctuations alone. In the special case $\chi = 0$, it takes the form

$$s_\rho(q) = -\frac{\left(q^2 - q_c^2\right)^2}{\tau q_c^4(1+2q^2)} + \frac{3q^2\rho_0^3\left(\zeta_\rho - \zeta_\rho^c\right)}{1+2q^2}. \tag{21}$$

The variable q_c denotes the wave number of the perturbation with the maximal growth rate s_ρ^m at the critical value $\zeta_\rho = \zeta_\rho^c$, where $s_\rho^m = 0$. It is given by

$$q_c = \frac{1}{[2\gamma A(\chi = 0)\tau]^{1/4}} \tag{22}$$

with $A = 3a\rho_0^2 - 5\chi/2$; see Appendix C 1. In turn, ζ_ρ^c is given by

$$\zeta_\rho^c = \frac{A(\chi = 0)}{3\rho_0} + \left(\sqrt{\frac{A(\chi = 0)\gamma}{3\rho_0^3}} + \sqrt{\frac{2}{3\rho_0^3\tau}}\right)^2. \tag{23}$$

This value provides a good approximation for ζ_ρ^c, when $\chi = 0.1$ [Fig. 5(a)].

Let us point out that the linear dynamics are qualitatively different in absence of renewal. In that case, density perturbations with $q = 0$ are marginal, implying a type II instability according to the classification of Cross and Hohenberg [49]. In contrast, the instability in the presence of renewal is of type I.

B. Nonlinear dynamics

To explore the system dynamics beyond linear stability, we numerically solved the dynamic equations (1)–(9) using a custom code written in Julia [50]. Details are given in Appendix D. The code can be found at [51]. Typically, we used square domains of size $L = 10$ with a discretization length $\Delta x = 10^{-2}$ and a total simulated time of 10^5. Selected simulations were run for a total simulated time of 2×10^6 or square domains of size $L = 50$. Units are set as described in Appendix B.

Simulations are initiated with a slight perturbation of the uniform disordered state by randomly perturbing both the uniform density, $\rho = \rho_0$, and the uniform polarity field, $\mathbf{p} = \mathbf{0}$. We observed a variety of different asymptotic behaviors. In the following we describe the different phases observed in the computations (Fig. 6).

1. Active foams

For target densities such as $\rho_0 = 0.7$ (Fig. 6 and Movie S9 [35]), the system organizes into a fully developed active foam: high-density edges form a connected network that encloses cells of lower density. At $\rho_0 = 0.4$ [Fig. 6(a) and Movie S6

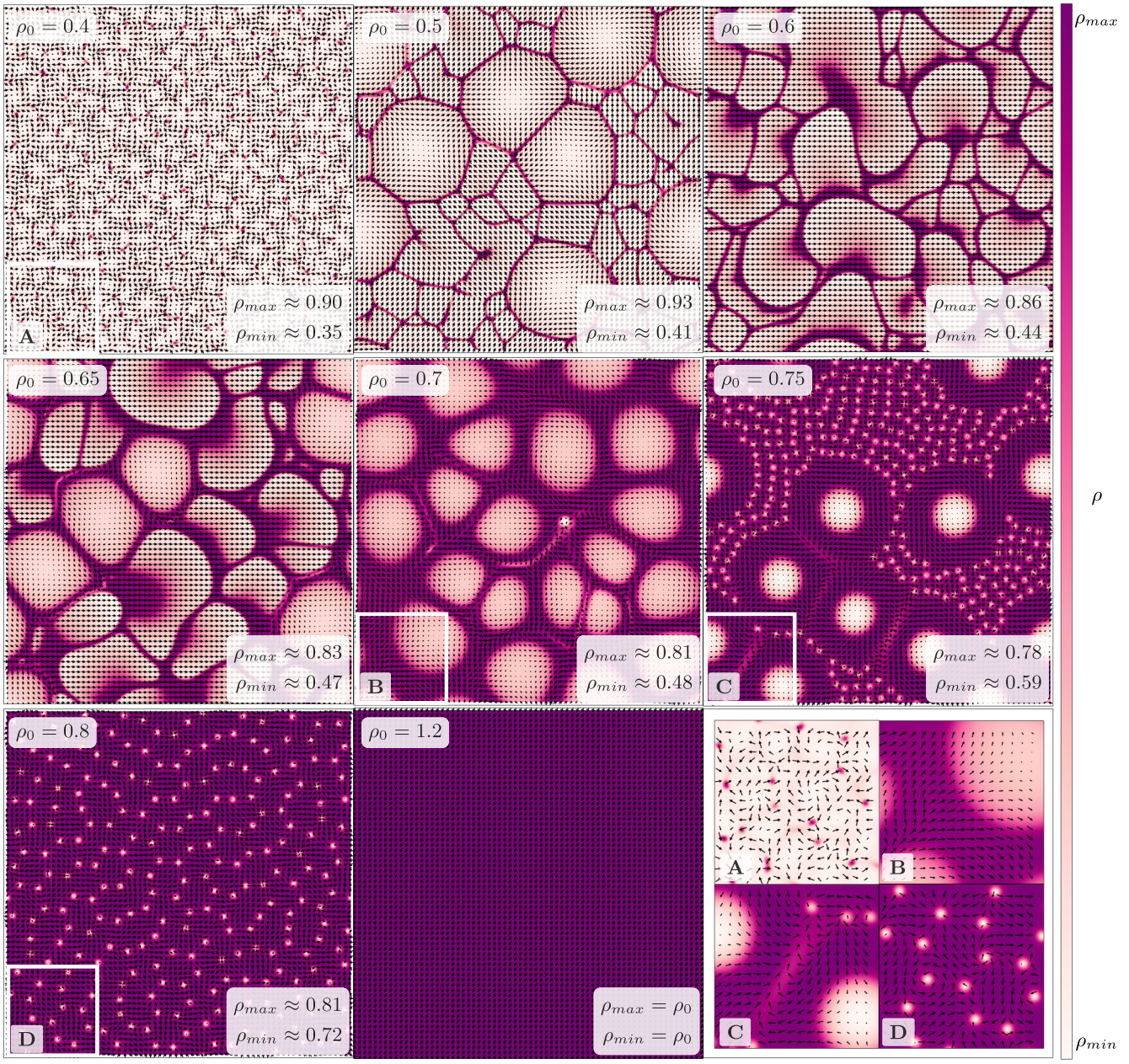


FIG. 6. Snapshots of the density (heatmaps) and polarity (black arrows) of asymptotic states of the dynamic equations (1)–(9) for different target densities ρ_0 for $\tau = 5$ and $\zeta_\rho = 4$. The system size is $L = 10$. Other parameters as in Table I. The same states are presented for a system of length $L = 50$ in Fig. S1 [35]. The bottom right panel shows zoomed-in views of selected snapshots, labeled A–D. Maximal and minimal densities are indicated in legends.

[35]], the system instead displays predominantly high-density puncta, which mark the vertices where the edges meet. The puncta are embedded in a background of density ρ_0, while the connecting edges and the enclosed cells are far less pronounced. Although the two snapshots look markedly different, our metrics identify them as the same physical phase, with similar defect densities and structural persistence times. In both cases the network is dynamic, undergoing constant rearrangements. We denote this phase an active foam and discuss its similarities and differences with active foam states reported in other systems in Sec. VI.

2. Density waves

As ρ_0 is increased further, traveling density waves appear, $\rho_0 = 0.6$ and $\rho_0 = 0.65$ in Fig. 6 and Movies S2 and S8 [35]. At the same time, uniform polar order emerges throughout the whole system. In contrast to lower densities, the cell shapes are elongated in one direction. The direction of elongation is on average perpendicular to the direction of motion of the density waves, but not correlated with the direction of the polarity field. These states are identical to the waves obtained when starting with a fully polarized state $\mathbf{p} = \mathbf{p}_0 = \text{const}$ with $|\mathbf{p}_0|^2 = 1$. At $\rho_0 = 0.7$ (Fig. 6 and Movie S9 [35]), we observe

reentrant behavior of active foams. This time the interfaces are thicker along the edges compared to active foams at lower densities [Fig. 6(b)]. This state also features traveling density waves.

3. Defect lattices

As the target density is increased further, the size of defect cores is again monodisperse. For densities around $\rho_0 = 0.8$, locally, regular defect lattices appear spontaneously [Fig. 6(d) and Movie S10 [35]]. The topological defects have charges of ± 1 and the lattices are either square or hexagonal. We discuss the lattice phase in more detail in Sec. V below, but mention that they need not be static and can move as a whole at constant velocity.

4. Homogeneous uniformly polarized state

For target densities ρ_0 beyond a critical value, the system asymptotically settles into a homogeneous state with uniform polarity (Movie S11 [35]). Indeed, the critical value ζ_ρ^c [Eq. (23)] increases with the density ρ_0. By increasing ρ_0 and keeping all other parameter values constant, the homogeneous uniformly polarized state becomes linearly stable. Our numerical results suggest that for sufficiently large densities ρ_0 the state is globally stable.

5. Coexistence of phases

Foams and waves. Not all of the states we observe correspond to a single, well-defined phase. In a range of intermediate target densities, our metrics instead resolve states in which two phases coexist. Between the foam and wave regimes we find two such coexistence regimes, which we refer to as foam-in-wave and wave-in-foam depending on which phase forms the connected background. With increasing target density ρ_0, the density along the edges increases; at $\rho_0 = 0.5$ (Fig. 6 and Movie S7 [35]) the system forms two sorts of cells. One kind contains a single integer topological defect of the polar order field, as in the active foam, whereas cells of the other kind contain no defect and the polarity is aligned throughout the cell, as in the wave phase. Some edges terminate in a vertex that is not connected to any other edge; this typically occurs in the defect-free cells. We therefore interpret this state as a coexistence of the foam and wave phases rather than as a distinct phase of its own.

Vortex glass. At a target density of $\rho_0 = 0.75$ (Fig. 6 and Movie S3 [35]), topological defects with cores of two distinct sizes emerge. The state is dynamic, with "small" defects flowing between "large" ones. Because of its resemblance to states found in the complex Ginzburg-Landau equation, we refer to this state as a vortex glass [52]. However, this state appears only in a narrow parameter window at the boundary between the foam and defect-lattice phases, and it combines characteristic features of both: the dynamic, continually rearranging network of the foams together with the regularly arranged defect cores of the lattices. We therefore interpret it not as an independent phase but as a coexistence of the foam and defect-lattice phases, and consequently it can be reached only by fine-tuning the parameters toward this phase boundary. As in the defect lattices, the charge $+1$ disclinations need not be vortices but can also be asters or spirals [Fig. 6(c)].

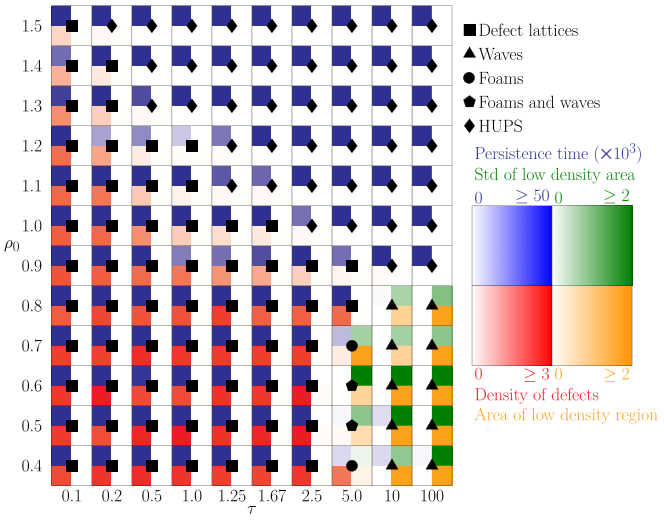


FIG. 7. Quantitative characterization of states as a function of the renewal parameters τ and ρ_0. Symbols: classification of states as in Sec. IV B. HUPS: homogeneous uniformly polarized state. Colors: defect density (red), structural persistence time T_p (blue), and mean $\langle A \rangle$ (yellow) and standard deviation σ_A of low-density surface areas (green); see text. Transparency decreases with higher values. There are no vortex glass states for the parameter values considered.

C. Quantitative characterization of states

To clarify the relation between the different states presented above, we introduce four quantities to quantitatively characterize them (Fig. 7). In addition to the defect density, we introduce the structural persistence time T_p as a measure of how dynamic the patterns are. To this end we consider the temporal correlation between density distributions at different times, where we take the maximum over all possible translations in space; see Appendix E for details. By considering the maximum correlation over translations of the density distribution, steady states and states moving with a constant drift velocity both have infinite structural persistence times.

Furthermore, we measure the extent of the low-density regions by the following procedure. First, we binarize the density field ρ by discriminating between regions with ρ below and above $\frac{9}{10}\langle\rho\rangle + \frac{1}{10}\min(\rho)$. This definition of the threshold value turned out to give a robust measure for distinguishing between different states. After segmenting space in this way, we consider the mean $\langle A \rangle$ and the standard deviation $\sigma_A = \langle A^2 \rangle - \langle A \rangle^2$ of the distribution of the low-density region surface areas; see Appendix E for details. These quantities distinguish, for example, defect lattices from waves and foams as the latter have typically much larger sized low-density regions and also waves from foams, where the former have a larger variance in the size of low-density regions.

We summarize these four quantities for varying values of the renewal parameters τ and ρ_0 in Fig. 7. The defect density decreases as τ and ρ_0 are increased. The intrinsic pattern correlation time is large (infinite) for defect lattices and homogeneous uniform polarized states. The former exist for target densities and renewal times below threshold values, whereas the latter require a minimum target density and renewal time. In the transition region from defects seas to homogeneous

uniform polarized states, defects move incoherently as in the vortex glass state.

Below a threshold target density ρ_0 and for large enough renewal times τ, the system generates density waves. Active foams exists in the transition region from defect seas to density waves. As the region of density waves is approached by increasing τ, the low-density regions expand, that is, $\langle A \rangle$ increases, which corresponds to the emergence of active foams. As the value of τ is increased further, states composed of foams and waves appear. We would like to point out that for $\tau = 5$, active foams exhibit reentrant behavior as ρ_0 is increased.

D. Competition between density and polarity perturbations

We can rationalize the transitions between the states in Fig. 6 as a function of the average density ρ_0 by comparing the rates associated with the fastest growing mode of density fluctuations λ_ρ^m and polarity fluctuations λ_p^m around the isotropic homogeneous state. The calculation of these two rates is given in Appendix C. For the parameters used in Fig. 6, we present their values as a function of ρ_0 in Fig. 5(b).

For intermediate target densities $\rho_0 \gtrsim 0.35$ and $\rho_0 \lesssim 0.7$, density fluctuations grow faster than polarity fluctuations [Fig. 5(b)]. Correspondingly, density patterns dominate in this parameter regime and impose polarity patterns (Fig. 6). With increasing average density ρ_0, the extent of the high-density domains increases.

Because the growth rate λ_p^m grows quadratically with ρ_0, whereas the growth rate λ_ρ^m is nonmonotonic with ρ_0, there is a crossover at about $\rho_0 \simeq 0.75$ to a regime where polarity fluctuations grow faster than density fluctuations [Fig. 5(b)]. In this case the final pattern results from the interaction between defects; see states at $\rho_0 = 0.75$ and $\rho_0 = 0.8$ in Fig. 6. At even larger target densities $\rho_0 > 0.85$, the system always relaxes to a polarized homogeneous phase (Fig. 6).

V. DEFECT LATTICES

In the defect lattices we described in the previous section, the topological defects in the polarity field locally arrange into regular polygons. This behavior is robust across varying parameter values. To further characterize these states, we performed longer simulations with a total time of $t = 2 \times 10^6$. Over time a global crystalline order of defect positions emerged (Fig. 8). We observed both square and hexagonal lattices [Figs. 8(a) and 8(c)].

Let us recall that numerical computations start from a slightly perturbed uniform disordered state. Due to local spontaneous symmetry breaking, defects in the polarity field appear throughout the system, initially forming an irregular arrangement. The defects created in this way are stabilized by the mechanism discussed in Sec. III and eventually arrange in a nearly disclination-free lattice as in Figs. 8(a) and 8(c). We checked that different initial conditions lead to the same final states up to rotation and translation (Fig. S3 and Table SI [35]).

A striking feature of these lattices is that they move at constant velocity without defect rearrangements (Movies S12 and S13 [35]). Defect lattices move at constant velocity along a direction that is not determined by the symmetry axes.

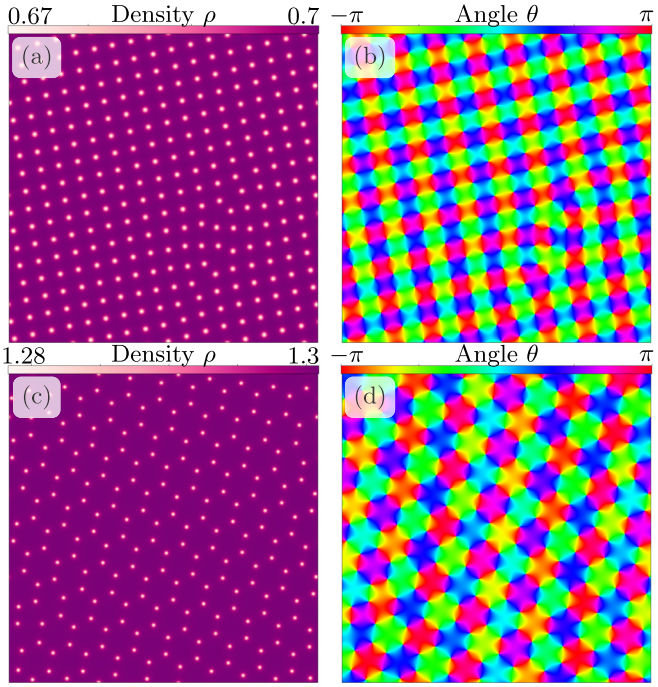


FIG. 8. Examples of square and hexagonal defect lattices. (a), (c) Density heatmaps at $t = 2 \times 10^6$ for $\rho_0 = 0.7$, $\tau = 1$, and $\zeta_\rho = 10$ (a) and for $\rho_0 = 1.3$, $\tau = 0.2$, and $\zeta_\rho = 1$ (c). (b), (d) Angle of the polarity field corresponding to (a) and (c). System size $L = 10$; other parameters as in Table I. The corresponding time evolution of the shape order Γ_p defined in Eq. (25) is given in Fig. S2 [35].

A detailed inspection of defect lattices reveals an alternating pattern of defects with topological charges $+1$ and -1 [Figs. 8(b) and 8(d) and Figs. S2(a) and S2(d) [35]. In the one-constant approximation, isolated $+1$ defects of either type—aster, spiral, and vortex—have the same total free energy [16]. Consistently, these subtypes appear in both, square and hexagonal defect lattices, but do not show any specific spatial organization [Figs. 8(b) and 8(d)].

The formation of defect lattices with clearly peaked structure factors takes too much time as if a thorough characterization of the corresponding phase space were feasible. To quantify the emerging crystalline order from shorter computer runs, we use the fact that the emergence of long-range translational order in the defect arrangement is preceded by long-range orientational order and use a method described in Ref. [10] for its quantification. We start by computing the Voronoi tesselation of defect centers, which assigns a polygonal cell to each defect based on its surrounding defects. From these polygons, we compute the shape function γ_p for $p = 1, 2, 3, \ldots$, which quantifies the degree of orientational order in the spatial arrangement of defect centers. Explicitly, for a single cell

$$\gamma_p = \frac{1}{\Delta_p} \sum_{v=1}^{V} |\mathbf{r}_v|^p \, e^{ip\phi_v}, \tag{24}$$

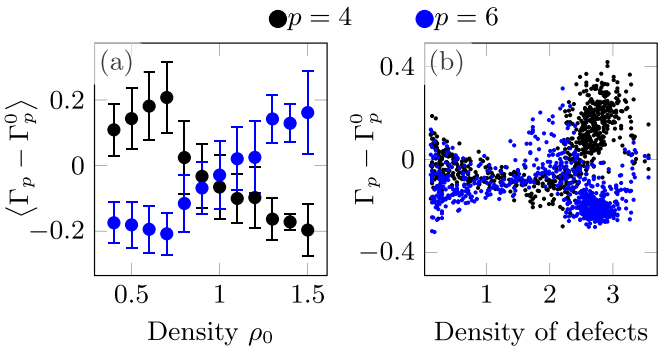


FIG. 9. Transition from square to hexagonal defect lattices. (a) Average of the shape function $\langle \Gamma_p - \Gamma_p^0 \rangle$ given by Eq. (25). For each value of ρ_0, the average is taken with respect to numerical solutions with $\tau = 0.1, 0.2, 0.5, 1, 1.2, 1.7, 2.5, 5, 10, 100$ and $\zeta_\rho = 0, 1, 2, 4, 6, \ldots, 24$. Only solutions with defect density larger than 1.5 were analyzed. (b) Shape function $\Gamma_p - \Gamma_p^0$ as a function of the defect density for the solutions used in (a). Error bars in panel (a) are SD. In both panels, the domain size $L = 10$.

where V is the number vertices of the cell, $\mathbf{r}_v$ the position of vertex v relative to the defect center, ϕ_v its angle with the x axis, and $\Delta_p = \sum_{v=1}^{V} |\mathbf{r}_v|^p$. For a regular p polygon, one has $\gamma_p = 1$, because $|\mathbf{r}_v| = \text{const}$ and because the angle between two adjacent vertices, $\measuredangle(\mathrm{r}_v, \mathrm{r}_{v+1})$, is $2\pi/p$. Finally, for each p, we average the absolute value of the shape function γ_p over all defect centers,

$$\Gamma_p = \langle |\gamma_p| \rangle. \tag{25}$$

To assess the degree of order, we compare Γ_p to Γ_p^0, its value for randomly distributed vertices, by computing the difference $\Gamma_p - \Gamma_p^0$.

The trajectories of $\Gamma_p - \Gamma_p^0$, which we computed for $p = 2, \ldots, 6$, indicate early on, $t \lesssim 10^5$, the developing crystalline order present in the arrangement of defects [Figs. S2(c) and S2(f) [35]). For each parameter set that displays a defect lattice, we use Γ_p at $t = 1.4 \times 10^5$ to characterize the organization of the defects. Although, in principle, this quantity can depend on the initial conditions, we find that it is essentially determined by the defect density [Fig. 9(b)]. Specifically, at sufficiently small defect densities, the dominant type of order is hexatic ($p = 6$). In contrast, at intermediate defect densities, the dominant order changes to quartic symmetry ($p = 4$), indicating that the emergence of quartic crystalline order is not an effect of packing constraints. This observation is further supported by defects with smaller cores arranging in triangular lattices, while those with bigger cores form square lattices. At intermediate defect densities (>1.5 per unit area), the crystalline order in the spatial arrangement of defect centers can also be controlled by the target density ρ_0 [Fig. 9(a)].

VI. DISCUSSION

In this work we studied the effect of renewal on the dynamics of active polar fluids with a focus on couplings between the density and polarity fields. Through a combination of extensive numerical computations and analytical calculations, we found various macroscopic phases, most notably active foams and defect lattices. The former are characterized by low-density regions surrounded by high-density interfaces, forming a dynamic network that continuously rearranges. The latter corresponds to arrays of integer topological defects that over time develop long-ranged crystal order, in particular triangular and square lattices. The topological defects are stabilized by an interplay between density gradients at the defect core and renewal. This mechanism is independent of the strength of the (anisotropic) active stress, unlike the mechanism for defect pair separation in active nematic fluids without renewal [48,53]. We find an overall similar behavior for active nematic fluids with renewal, which we report elsewhere. In active fluids with mixed nematic and polar orientational order, new structures, for example, stable topological strings appear [54].

Renewal is a generic feature of living matter, on subcellular [55–57] as well as tissue scales [58–60]. We expect our findings to be particularly relevant for cellular processes involving the actin cortex and tissue homeostasis. Some the states similar to those we have reported above have been described in cytoskeletal and multicellular systems.

An active foam state has been reported in three-dimensional microtubule-motor mixtures [61]. Motor accumulation at microtubule ends is an important feature of this state. As our theory does not distinguish between filaments and motors, it is not obvious how to relate this experimental feature to our theory. Furthermore, in the experiment, the accumulation of motors at microtubule ends rather leads to high motor-filament densities in asters, which is opposite to the depletion of active fluid generated by the free energy density (1). With respect to multicellular systems, nonconfluent tissues seem to be interesting candidates for active foam states. Even in this case, orientational order can be observed in tissues, either in the presence of a structured substrate [62] or not [6].

Theoretically, a contractile network with some similarity to the active foam state has been obtained in Ref. [63]. In that work renewal of the active fluid is assumed to be regulated by biochemical reactions. However, in that description, the active fluid is isotropic and the contractile network eventually approaches a stationary state. In addition, an active foam state has been reported for so-called Malthusian flocks of self-propelled particles in the limit of constant density [64]. There the "bubbles" of the foam are delimited by line defects in the orientational order field.

Cytoplasmic compartmentalization by microtubule asters in frog extracts and zebrafish embryos exhibit spatial and orientational order that is comparable to foam states or defects lattices [65,66]. The interplay between renewal and elastic stress or active stress might thus be a key ingredient for partitioning the cytoplasm in syncytia [67]. The density distribution of the states reported above is, however, inverted with respect to the experimentally observed arrangements. If and if yes, how our description can be modified to appropriately capture the mechanism underlying compartmentalization in these systems remains to be seen.

There have been a number of theoretical works on defect lattices in active fluids [29–31,68–71]. In two-dimensional nematic active fluids, defect lattices were notably reported in the case of high surface friction compared to internal friction [30,31,71]. In these works the active anisotropic stress was

extensile. As we have shown in Sec. III, in our polar fluid, renewal leads to a repulsive interaction between defects in the absence of active stress and even in the presence of contractile activity. In Ref. [72], a lattice of density maxima was reported in an active nematic. There, nematic order is perfectly aligned in regions of high density.

We would like to point out that we restricted our analysis to the simplest form of renewal, which depends linearly on the fluid density. In the presence of nonlinear terms, as long as the density remains everywhere in the basin of attraction of the target density, we expect the dynamics to remain qualitatively the same as in the linear case. We have checked this explicitly for quadratic terms in the renewal dynamics. In general, however, phenomena in addition to those reported in this present work might be observed. Instead of a systematic study of the effects of nonlinear terms in the renewal dynamics, we suggest to focus on specific nonlinear terms based on experimental observations.

A potentially more interesting modification of the renewal dynamics is by including biochemical regulation as already alluded to above. Indeed, qualitatively distinct states and new dynamics has been reported, when such regulation is included in the description [63,73–76]. Also experimentally interesting dynamics of proteins regulating cytoskeletal renewal have been observed [77,78]. In future work, it will be interesting to study the effects of couplings between biochemical regulation and the dynamics of active fluids in the presence of renewal.

Coupling to biochemical signaling networks is not the only way to generate heterogeneous renewal. In tissues, cell division and death depends on cell density [79,80]. Alternatively, cell division and death can depend on the stress in the fluid [81,82]. This is also true for the renewal of actin filaments [83]. Such situations could be captured by introducing a stress dependence in the assembly or disassembly rates, for example, similar as in Ref. [83]. Finally, renewal dynamics could be localized or accelerated at boundaries [84]. Such effects could be captured by appropriate boundary conditions [38,85]. Alternatively, a phase field can be introduced to distinguish between the in- and outside of a cell or a tissue. This approach is of particular interest, when the boundary is itself dynamic [86,87]. The special conditions at the boundary are then be captured by turnover rates that depend on phase-field gradients.

Our work highlights renewal as a fundamental ingredient of active matter, capable of qualitatively altering its collective dynamics and giving rise to emergent states that are inaccessible in systems with conserved mass. We therefore expect that explicitly accounting for renewal will prove essential for understanding the organization and dynamics of living matter across scales.

ACKNOWLEDGMENTS

L.D. and K.K. gratefully acknowledge funding by Swiss National Science Foundation (Grant No. 200020E_219164). Numerical solutions of the dynamic equations were performed at the University of Geneva's Baobab HPC cluster.

DATA AVAILABILITY

The custom code to generate and analyze the data as well as the data for all figures are publicly available [51].

APPENDIX A: EXPRESSIONS FOR THE CHEMICAL POTENTIAL, MOLECULAR FIELD, AND ERICKSEN STRESS

In this section we give the explicit expressions of the chemical potential $\mu = \frac{\delta \mathcal{F}}{\delta \rho}$, the molecular field $\mathbf{h} = -\frac{\delta \mathcal{F}}{\delta \mathbf{p}}$, and the Ericksen stress $\sigma^{\mathrm{e}}_{\alpha\beta}$ given by Eq. (2). The total free energy is $\mathcal{F} = \int f d\mathbf{r}$, where $d\mathbf{r}$ is an infinitesimal area element and f is the free-energy density given by Eq. (1). We obtain

$$\mu = a\rho^3 + \rho\left(-\frac{3}{2}\chi\frac{\rho}{\rho_0}p_\gamma^2 + \frac{1}{2}\chi\left(p_\gamma^2\right)^2 + \kappa(\partial_\gamma p_\delta)^2\right), \tag{A1}$$

$$h_\alpha = \chi\rho^2\left(\frac{\rho}{\rho_0} - p_\gamma^2\right)p_\alpha + \kappa\partial_\beta(\rho^2\partial_\beta p_\alpha), \tag{A2}$$

$$\sigma^{\mathrm{e}}_{\alpha\beta} = -\left[\frac{3}{4}a\rho^4 - \rho^2\left(\chi\frac{\rho}{\rho_0}p_\gamma^2 - \frac{1}{4}\chi\left(p_\gamma^2\right)^2\right)\right]\delta_{\alpha\beta} - \rho^2\left[\frac{1}{2}\kappa(\partial_\gamma p_\delta)^2\right]\delta_{\alpha\beta} - \kappa\rho^2(\partial_\alpha p_\gamma)(\partial_\beta p_\gamma). \tag{A3}$$

APPENDIX B: DIMENSIONLESS EQUATIONS

Let us begin by defining the units used in our theoretical description. The time unit is set by an arbitrary timescale T, the length scale by $\lambda = \sqrt{\eta\xi^{-1}}$, and the viscosity scale by η. Combining these expressions, we define a density scale as $\tilde{\rho} = \eta T\lambda^{-2}$.

In this unit system, the dimensionless parameters are $a' = a\tilde{\rho}^4 T\eta^{-1}$, $\chi' = \chi\tilde{\rho}^2 T\eta^{-1}$, $\kappa' = \kappa\tilde{\rho}^2 T\eta^{-1}\lambda^{-2}$, $\rho_0' = \rho_0\tilde{\rho}^{-1}$, $\tau' = \tau T^{-1}$, $\nu' = \nu$, $\zeta_\rho' = \zeta_\rho\tilde{\rho}^3 T\eta^{-1}$, $\zeta_p' = \zeta_p\tilde{\rho}T\eta^{-1}$, $\gamma' = \gamma\eta\lambda^{-2}\tilde{\rho}^{-2}$, and $\Gamma' = \Gamma\eta^{-1}$.

Finally, we set $\Delta\mu = 1$ to simplify the notation.

APPENDIX C: LINEAR STABILITY ANALYSIS OF THE HOMOGENEOUS STATE

In this section we present the linear stability analysis of two homogeneous states: the polarized state and the isotropic state. We focus on the special case with no flow alignment, $\nu = 0$ and no anisotropic stress, $\zeta_p = 0$.

1. Polarized homogeneous state

To study the linear stability of the polarized state, we consider without limiting generality that the polar field is aligned along the x axis, $\mathbf{p}_0.\mathbf{e}_y = 0$. We set $\rho = \rho_0 + \delta\rho$, $\mathbf{p} = \mathbf{p}_0 + \delta\mathbf{p}$ with $|\mathbf{p}_0| = 1$, and $\mathbf{v} = \delta\mathbf{v}$, and derive the dynamic equations to first order in the perturbations $\delta\rho$, $\delta\mathbf{p}$, and $\delta\mathbf{v}$. By setting $\delta\rho = \hat{\rho}(q_x, q_y)e^{i(q_x x + q_y y)}$ and similarly defining the Fourier components $\hat{v}_x$ and $\hat{v}_y$ for the velocity perturbation $\delta\mathbf{v}$ and $\hat{p}_x$ and $\hat{p}_y$ for the polarity perturbation, we use force balance (5) to express $\hat{v}_x$ and $\hat{v}_y$ in terms of $\hat{\rho}$, $\hat{p}_x$, and $\hat{p}_y$. Explicitly,

$$\hat{v}_x = \frac{-iq_x\rho_0}{2q^2+1}[(A - 3\rho_0\zeta_\rho)\hat{\rho} - \chi\rho_0\hat{p}_x] - \frac{1}{2}\frac{iq_y q^2\rho_0^2}{q^2+1}\kappa\hat{p}_y, \tag{C1}$$

$$\hat{v}_y = \frac{-iq_y\rho_0}{2q^2+1}[(A - 3\rho_0\zeta_\rho)\hat{\rho} - \chi\rho_0\hat{p}_x] + \frac{1}{2}\frac{iq_x q^2\rho_0^2}{q^2+1}\kappa\hat{p}_y. \tag{C2}$$

Here, as in the main text, $A = 3a\rho_0^2 - \frac{5}{2}\chi > 0$ and $q^2 = q_x^2 + q_y^2$ denotes the squared magnitude of the wave vector $\mathbf{q} = (q_x, q_y)$.

Substituting the expressions for $\hat{v}_x$ and $\hat{v}_y$ into the linearized equations (1)–(9), we obtain, to linear order in perturbations, the following dynamical equations for the density and the polarization:

$$\partial_t \hat{\rho} = -[\tau^{-1} + B(q)]\hat{\rho} + C(q)\hat{p}_x, \tag{C3}$$

$$\partial_t \hat{p}_x = \frac{\chi\rho_0}{\Gamma}\hat{\rho} - \rho_0^2\frac{2\chi + \kappa q^2}{\Gamma}\hat{p}_x, \tag{C4}$$

$$\partial_t \hat{p}_y = -\kappa\rho_0^2 q^2\left(\frac{1}{\Gamma} + \frac{1}{4}\frac{q^2}{q^2+1}\right)\hat{p}_y \tag{C5}$$

with $B(q) = q^2[\rho_0^2(A - 3\rho_0\zeta_\rho)/(1+2q^2) + \gamma A]$ and $C(q) = q^2\chi\rho_0[\rho_0^2/(1+2q^2) + \gamma]$. Note that perturbations in the polarization component perpendicular to the x axis p_y always decay, as shown by Eq. (C5). The linear dynamics of perturbations in ρ and p_x are in general coupled, and the resulting expressions for the two associated growth rates are rather involved, such that we do not present them here. However, valuable insights can be gained by considering the special case $\chi = 0$, in which the linear dynamics of ρ and p_x decouple. In this case, perturbations in p_x always decay [see Eq. (C4)], while perturbations in ρ evolve with a growth rate s_ρ, $\delta\rho \sim e^{s_\rho t}$, which can be recast in the form

$$s_\rho(q) = -\frac{\left(q^2 - q_c^2\right)^2}{\tau q_c^4(1+2q^2)} + \frac{3q^2\rho_0^3\left(\zeta_\rho - \zeta_\rho^c\right)}{1+2q^2}. \tag{C6}$$

The variable q_c denotes the wave number of the perturbation with the maximal growth rate s_ρ^m at the critical value $\zeta_\rho = \zeta_\rho^c$, where $s_\rho^m = 0$, and is given by

$$q_c = \frac{1}{(2\gamma A(\chi=0)\tau)^{1/4}}. \tag{C7}$$

The critical value ζ_ρ^c of the active stress for which $s_\rho^m = 0$ at $q = q_c$ vanishes is given by

$$\zeta_\rho^c = \frac{A(\chi=0)}{3\rho_0} + \left(\sqrt{\frac{A(\chi=0)\gamma}{3\rho_0^3}} + \sqrt{\frac{2}{3\rho_0^3\tau}}\right)^2. \tag{C8}$$

2. Isotropic homogeneous state

In the following, we present the linear stability analysis of the isotropic homogeneous state. This state with a small random perturbation was used in our numerical integration of Eqs. (1)–(9).

We set $\rho = \rho_0 + \delta\rho$, $\mathbf{p} = \delta\mathbf{p}$, and $\mathbf{v} = \delta\mathbf{v}$, and derive the dynamic equations to first order in the perturbations $\delta\rho$, $\delta\mathbf{p}$, and $\delta\mathbf{v}$. In Fourier space (see previous section), we use force balance (5) to express $\hat{v}_x$ and $\hat{v}_y$ in terms of $\hat{\rho}$, $\hat{p}_x$, and $\hat{p}_y$. Explicitly,

$$\hat{v}_x = 3E\frac{iq_x}{2q^2+1}\hat{\rho}, \tag{C9}$$

$$\hat{v}_y = 3E\frac{iq_y}{2q^2+1}\hat{\rho} \tag{C10}$$

with $q^2 = q_x^2 + q_y^2$ and $E = (\zeta_\rho - a\rho_0)\rho_0^2$. Substituting the expressions above for $\hat{v}_x$ and $\hat{v}_y$ into the linearized equations (1)–(9), we obtain the following dynamical equations for the density and the polarization:

$$\frac{d}{dt}\hat{\rho} = -\left\{\frac{1}{\tau} + 3q^2\left[a\rho_0^2\gamma - \rho_0\frac{E}{2q^2+1}\right]\right\}\hat{\rho}, \tag{C11}$$

$$\frac{d}{dt}\hat{\mathbf{p}} = \frac{\rho_0^2}{\Gamma}(\chi - \kappa q^2)\hat{\mathbf{p}}. \tag{C12}$$

As long as $\chi > 0$, the isotropic state is unstable to perturbations in the polarity field, with a growth rate increasing quadratically with the target density ρ_0.

In Fig. 5 we represent the growth rates s_ρ^m and s_p^m associated with the fastest growing modes of density and polarity perturbations of the isotropic homogeneous state. These rates were calculated using (C11) and (C12). The rate $s_p^m = \chi\rho_0^2/\Gamma$ is quadratic in the target density ρ_0^2, but independent of the elastic coefficient κ.

APPENDIX D: NUMERICAL METHODS

In this appendix we provide some details on the numerical used to integrate (1)–(9). The code is available at [51].

Spatial derivatives were calculated by first transforming the dynamic fields to the reciprocal space using the two-dimensional Fast Fourier Transform (FFT) technique, then multiplication with the corresponding wave vectors and, finally, transforming back to real space using FFT. Temporal integration was executed through the explicit Euler forward method. The computational grid encompassed at least 1008×1008 discrete points, with a spatial discretization of $\Delta x = 10^{-2}$. The maximal temporal discretization is set to $\Delta t_{\max} = 10^{-2}$ and Δt is chosen at every time unit Δt according to the rule $\Delta t = \min\{\Delta t_{\max}, 5\times10^{-2}\Delta x/\max(||v||), 1.25\Delta t_{\text{prev}}\}$ with Δt_{prev} being the previous time step. These computations were performed on GPUs.

At each time step, the chemical potential μ [Eq. (A1)], the molecular field h_α [Eq. (A2)], and the total stress minus the viscous stress $\sigma_{\alpha\beta}^{\text{nv}} = \sigma_{\alpha\beta}^{\text{tot}} - 2\eta v_{\alpha\beta}$, were computed in real space. Then the velocity field was computed by solving the force balance [Eq. (5)] in Fourier space. Finally, the temporal the density and polarity fields were updated by time integration of Eqs. (4) and (9).

APPENDIX E: IDENTIFICATION AND CHARACTERIZATION OF PHASES

To characterize the various asymptotic states of the dynamics, we monitor four observables: the density of topological defects, the average size of low-density regions along with its standard deviation, and the structural persistence time T_p. The latter serves as a measure of structural persistence, which quantifies the time period over which a spatial configuration of the density field remains autocorrelated.

The number of defects N_{def} is determined by identifying the regions, where $|\mathbf{p}|^2 < p_{\max}/4$, where $p_{\max}$ is the maximum polarization amplitude, and then counting the number of these regions. The density of defects is defined as $n_{\text{def}} = N_{\text{def}}/L^2$.

To obtain the distribution of the areas of the low-density regions, we analyze the density field over a series of snapshots

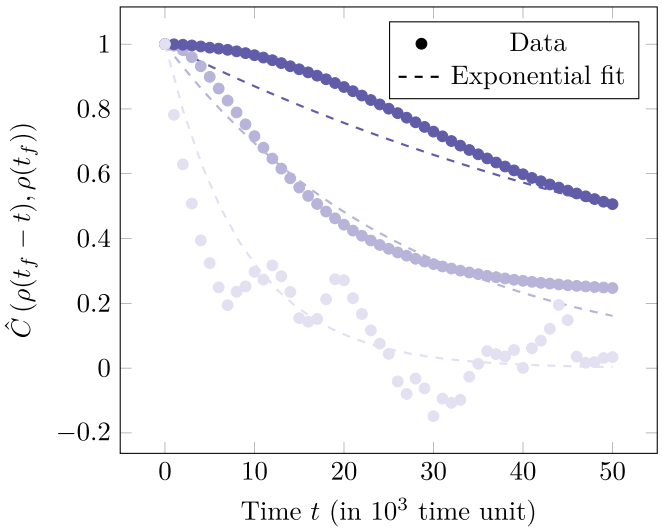


FIG. 10. Examples of the correlation function $\hat{C}(t)$ for $\rho_0 = 0.7$, $\tau = 1$, and $T_p = 7.2 \times 10^4$ (dark blue), $\rho_0 = 1.2$, $\tau = 0.5$, and $T_p = 2.7 \times 10^4$ (lighter blue), and $\rho_0 = 0.7$, $\tau = 5$, and $T_p = 8.8 \times 10^3$ (lightest blue). Dots: numerical data, dashed lines: exponential fit. In all cases, $t_f = 287 \times 10^3$. Other parameter values as in Table I.

at the end of a numerical solution. The solutions were evolved for long enough to have converged to the asymptotic solution. Each snapshot is first extended periodically to respect the boundary conditions. We then binarize the field, labeling as low-density every pixel with ρ below the threshold $\rho^* = \frac{9}{10}\langle\rho\rangle + \frac{1}{10}\min(\rho)$; snapshots with negligible density contrast ($\max\rho - \min\rho < 10^{-5}$) are treated as uniform and discarded. Since adjacent low-density regions can be connected through narrow necks, we separate them using a Euclidean distance transform, assigning to each low-density pixel its distance to the nearest high-density pixel and retaining the resulting cores. These cores are segmented into individual regions with the Felzenszwalb algorithm (scale parameter $k = 5$, minimum region size 50 pixels), and the pixel count of each segment is converted into a physical area through the grid spacing. The single largest region, corresponding to the system-spanning background, is discarded. Aggregating the areas of all remaining regions over every snapshot yields the distribution, from which we compute the mean $\langle A\rangle$ and standard deviation σ_A.

TABLE II. Classification criteria for homogeneous uniformly polarized states (HUPS), defect lattices, foams, waves and mixed states based on the defect density n_{def}, the average area of low-density regions $\bar{A}$, the corresponding standard deviation σ_A, and the structural persistence time T_p.

	n_{def}	$\langle A\rangle$	σ_A	T_p
HUPS	~ 0	$\emptyset$	$\emptyset$	$\to\infty$
Defect lattices	>0	$\in]0, 0.5]$	$<\bar{A}$	$\gg 10^4$
Foams	>0	$\in]0.5, L/4]$	$<\bar{A}$	$<2.5 \times 10^3$
Waves	0	$\in]0.5, L/4]$	$<\bar{A}$	$<2.5 \times 10^3$
Foams + Waves	>0	$\in]0.5, L/4]$	$>\bar{A}$	$<2.5 \times 10^3$
Foams + Lattices	>0	$\in]0, 0.5]$	$>\bar{A}$	$\gg 10^4$

Finally, the structural persistence time T_p is computed using the correlation between the fluctuations of the two density fields ρ and ρ', $C(\rho, \rho')$.

$$C(\rho, \rho') = \begin{cases} \frac{\langle \delta\rho \times \delta\rho' \rangle}{\sqrt{\langle \delta\rho^2 \rangle \langle \delta\rho'^2 \rangle}}, & \langle|\delta\rho|\rangle < 10^{-6}, \langle|\delta\rho'|\rangle < 10^{-6} \\ 1, & \text{otherwise} \end{cases}$$

where the fluctuation of the density field ρ is defined as $\delta\rho = \rho - \langle\rho\rangle$, and $\langle\times\rangle$ denotes spatial averaging over the system. Since patterns can move with a constant velocity, we also consider the correlation with translated patterns. Specifically, let $\mathcal{T}\rho$ denote the density ρ after performing a translation $\mathcal{T}$ over a discrete space of $[-3, 3]$ pixels. We define $\hat{C}(t) \equiv \max_{\mathcal{T}} C(\rho(t_f), \mathcal{T}\rho(t_f - t))$. Here t_f denotes the final time of a numerical solution. Asymptotically, we expect $\hat{C}(t) \sim \exp(-t/T_p)$. Although, numerically, our correlation functions deviate from this expectation, we still fit an exponential to the data to obtain a value for T_p (Fig. 10).

These quantities provide a comprehensive characterization of the system, enabling a clear distinction between regimes defined by defect concentration, the fragmentation of low-density domains, and the persistence of dynamical structures. The specific criteria used for identifying the different states are given in Table II.

[1] J. Prost, F. Jülicher, and J. F. Joanny, Active gel physics, Nat. Phys. **11**, 111 (2015).
[2] A. B. Verkhovsky, T. M. Svitkina, and G. G. Borisy, Self-polarization and directional motility of cytoplasm, Curr. Biol. **9**, 11 (1999).
[3] A. C. Martin, M. Kaschube, and E. F. Wieschaus, Pulsed contractions of an actin-myosin network drive apical constriction, Nature (London) **457**, 495 (2009).
[4] M. Mayer, M. Depken, J. S. Bois, F. Jülicher, and S. W. Grill, Anisotropies in cortical tension reveal the physical basis of polarizing cortical flows, Nature (London) **467**, 617 (2010).
[5] T. Sanchez, D. T. N. Chen, S. J. DeCamp, M. Heymann, and Z. Dogic, Spontaneous motion in hierarchically assembled active matter, Nature (London) **491**, 431 (2012).
[6] G. Duclos, S. Garcia, H. G. Yevick, and P. Silberzan, Perfect nematic order in confined monolayers of spindle-shaped cells, Soft Matter **10**, 2346 (2014).
[7] F. J. Ndlec, T. Surrey, A. C. Maggs, and S. Leibler, Self-organization of microtubules and motors, Nature (London) **389**, 305 (1997).
[8] M. Delarue, J.-F. Joanny, F. Jülicher, and J. Prost, Stress distributions and cell flows in a growing cell aggregate, Interface Focus **4**, 20140033 (2014).
[9] S. Jain, V. M. L. Cachoux, G. H. N. S. Narayana, S. de Beco, J. D'Alessandro, V. Cellerin, T. Chen, M. L. Heuzé, P. Marcq, R.-M. Mège, A. J. Kabla, C. T. Lim, and B. Ladoux, The role of single-cell mechanical behaviour and polarity in driving collective cell migration, Nat. Phys. **16**, 802 (2020).

[10] J.-M. Armengol-Collado, L. N. Carenza, J. Eckert, D. Krommydas, and L. Giomi, Epithelia are multiscale active liquid crystals, Nat. Phys. **19**, 1773 (2023).
[11] M. Dedenon and K. Kruse, Noise-induced transitions from contractile to extensile active stress in isotropic fluids, Phys. Rev. E **111**, 015426 (2025).
[12] T. B. Saw, A. Doostmohammadi, V. Nier, L. Kocgozlu, S. Thampi, Y. Toyama, P. Marcq, C. T. Lim, J. M. Yeomans, and B. Ladoux, Topological defects in epithelia govern cell death and extrusion, Nature (London) **544**, 212 (2017).
[13] K. Kawaguchi, R. Kageyama, and M. Sano, Topological defects control collective dynamics in neural progenitor cell cultures, Nature (London) **545**, 327 (2017).
[14] Y. Maroudas-Sacks, L. Garion, L. Shani-Zerbib, A. Livshits, E. Braun, and K. Keren, Topological defects in the nematic order of actin fibres as organization centres of *Hydra* morphogenesis, Nat. Phys. **17**, 251 (2021).
[15] P. Guillamat, C. Blanch-Mercader, G. Pernollet, K. Kruse, and A. Roux, Integer topological defects organize stresses driving tissue morphogenesis, Nat. Mater. **21**, 588 (2022).
[16] P. G. de Gennes and J. Prost, *The Physics of Liquid Crystals*, 2nd ed. (Oxford University Press, Oxford, 2002).
[17] A. J. Vromans and L. Giomi, Orientational properties of nematic disclinations, Soft Matter **12**, 6490 (2016).
[18] X. Tang and J. V. Selinger, Orientation of topological defects in 2D nematic liquid crystals, Soft Matter **13**, 5481 (2017).
[19] D. J. G. Pearce and K. Kruse, Properties of twisted topological defects in 2D nematic liquid crystals, Soft Matter **17**, 7408 (2021).
[20] C. Blanch-Mercader, P. Guillamat, A. Roux, and K. Kruse, Quantifying material properties of cell monolayers by analyzing integer topological defects, Phys. Rev. Lett. **126**, 028101 (2021).
[21] Y. Maroudas-Sacks, L. Garion, S. Suganthan, M. Popović, and K. Keren, Confinement modulates axial patterning in regenerating Hydra, PRX Life **2**, 043007 (2024).
[22] Y. Ravichandran, M. Vogg, K. Kruse, D. J. G. Pearce, and A. Roux, Topology changes of *Hydra* define actin orientation defects as organizers of morphogenesis, Sci. Adv. **11**, eadr9855 (2025).
[23] S. P. Thampi, R. Golestanian, and J. M. Yeomans, Velocity correlations in an active nematic, Phys. Rev. Lett. **111**, 118101 (2013).
[24] L. Giomi, Geometry and topology of turbulence in active nematics, Phys. Rev. X **5**, 031003 (2015).
[25] R. Alert, J. Casademunt, and J.-F. Joanny, Active turbulence, Annu. Rev. Condens. Matter Phys. **13**, 143 (2022).
[26] D. J. G. Pearce, Activity driven orientational order in active nematic liquid crystals on an anisotropic substrate, Phys. Rev. Lett. **122**, 227801 (2019).
[27] D. J. G. Pearce, Defect order in active nematics on a curved surface, New J. Phys. **22**, 063051 (2020).
[28] K. Thijssen and A. Doostmohammadi, Binding self-propelled topological defects in active turbulence, Phys. Rev. Res. **2**, 042008(R) (2020).
[29] A. U. Oza and J. Dunkel, Antipolar ordering of topological defects in active liquid crystals, New J. Phys. **18**, 093006 (2016).
[30] A. Doostmohammadi, M. F. Adamer, S. P. Thampi, and J. M. Yeomans, Stabilization of active matter by flow-vortex lattices and defect ordering, Nat. Commun. **7**, 10557 (2016).
[31] K. Thijssen, M. R. Nejad, and J. M. Yeomans, Role of friction in multidefect ordering, Phys. Rev. Lett. **125**, 218004 (2020).
[32] S. Shankar, A. Souslov, M. J. Bowick, M. C. Marchetti, and V. Vitelli, Topological active matter, Nat. Rev. Phys. **4**, 380 (2022).
[33] T. B. Saw, W. Xi, B. Ladoux, and C. T. Lim, Biological tissues as active nematic liquid crystals, Adv. Mater. **30**, 1802579 (2018).
[34] Y. Maroudas-Sacks and K. Keren, Mechanical patterning in animal morphogenesis, Annu. Rev. Cell Dev. Biol. **37**, 469 (2021).
[35] See Supplemental Material at http://link.aps.org/supplemental/10.1103/bnx5-sryc for Figures S1–S3, Table SI, and Movies S1–S13.
[36] J. F. Joanny, F. Jülicher, K. Kruse, and J. Prost, Hydrodynamic theory for multi-component active polar gels, New J. Phys. **9**, 422 (2007).
[37] A. C. Callan-Jones and F. Jülicher, Hydrodynamics of active permeating gels, New J. Phys. **13**, 093027 (2011).
[38] J. F. Joanny, K. Kruse, J. Prost, and S. Ramaswamy, The actin cortex as an active wetting layer, Eur. Phys. J. E **36**, 52 (2013).
[39] R. M. Adar and J.-F. Joanny, Active-gel theory for multicellular migration of polar cells in the extra-cellular matrix, New J. Phys. **24**, 073001 (2022).
[40] K. Kruse, J.-F. Joanny, F. Jülicher, J. Prost, and K. Sekimoto, Asters, vortices, and rotating spirals in active gels of polar filaments, Phys. Rev. Lett. **92**, 078101 (2004).
[41] B. I. Shraiman, Mechanical feedback as a possible regulator of tissue growth, Proc. Natl. Acad. Sci. USA **102**, 3318 (2005).
[42] M. Basan, T. Risler, J.-F. Joanny, X. Sastre-Garau, and J. Prost, Homeostatic competition drives tumor growth and metastasis nucleation, HFSP J. **3**, 265 (2009).
[43] S. R. de Groot and P. Mazur, *Non-Equilibrium Thermodynamics* (Dover Publications, New York, 1984).
[44] Y. Mori, K. Matsumoto, T. Ueda, and Y. Kobatake, Spatio-temporal organization of intracellular ATP content and oscillation patterns in response to blue light by *Physarum polycephalum*, Protoplasma **135**, 31 (1986).
[45] K. Kruse, J.-F. Joanny, F. Jülicher, J. Prost, and K. Sekimoto, Generic theory of active polar gels: A paradigm for cytoskeletal dynamics, Eur. Phys. J. E **16**, 5 (2005).
[46] N. Levernier and K. Kruse, Spontaneous formation of chaotic protrusions in a polymerizing active gel layer, New J. Phys. **22**, 013003 (2020).
[47] L. Giomi, M. J. Bowick, X. Ma, and M. C. Marchetti, Defect annihilation and proliferation in active nematics, Phys. Rev. Lett. **110**, 228101 (2013).
[48] L. Giomi, M. J. Bowick, P. Mishra, R. Sknepnek, and M. Cristina Marchetti, Defect dynamics in active nematics, Phil. Trans. R. Soc. A **372**, 20130365 (2014).
[49] M. C. Cross and P. C. Hohenberg, Pattern formation outside of equilibrium, Rev. Mod. Phys. **65**, 851 (1993).
[50] J. Bezanson, A. Edelman, S. Karpinski, and V. B. Shah, Julia: A fresh approach to numerical computing, SIAM Rev. **59**, 65 (2017).
[51] L. Dumoulin, C. Blanch-Mercader, and K. Kruse, Solver for active polar fluids with renewal (Version v1.0.0) [Computer software], Zenodo, 2026, https://doi.org/10.5281/zenodo.23065285.
[52] C. Brito, I. S. Aranson, and H. Chaté, Vortex glass and vortex liquid in oscillatory media, Phys. Rev. Lett. **90**, 068301 (2003).

[53] S. Shankar, S. Ramaswamy, M. C. Marchetti, and M. J. Bowick, Defect unbinding in active nematics, Phys. Rev. Lett. **121**, 108002 (2018).
[54] A. Dinelli, L. Dumoulin, and K. Kruse, Active topological strings in renewing nematopolar fluids, arXiv:2601.18307.
[55] T. D. Pollard, L. Blanchoin, and R. D. Mullins, Molecular mechanisms controlling actin filament dynamics in nonmuscle cells, Annu. Rev. Biophys. Biomol. Struct. **29**, 545 (2000).
[56] T. Lecuit and P.-F. Lenne, Cell surface mechanics and the control of cell shape, tissue patterns and morphogenesis, Nat. Rev. Mol. Cell Biol. **8**, 633 (2007).
[57] B. L. Goode, J. Eskin, and S. Shekhar, Mechanisms of actin disassembly and turnover, J. Cell Biol. **222**, e202309021 (2023).
[58] B. Simons and H. Clevers, Strategies for homeostatic stem cell self-renewal in adult tissues, Cell **145**, 851 (2011).
[59] S. A. Gudipaty and J. Rosenblatt, Epithelial cell extrusion: Pathways and pathologies, Semin. Cell Dev. Biol. **67**, 132 (2017).
[60] L. E. O'Brien, Tissue homeostasis and non-homeostasis: From cell life cycles to organ states, Annu. Rev. Cell Dev. Biol. **38**, 395 (2022).
[61] B. Lemma, N. P. Mitchell, R. Subramanian, D. J. Needleman, and Z. Dogic, Active microphase separation in mixtures of microtubules and tip-accumulating molecular motors, Phys. Rev. X **12**, 031006 (2022).
[62] Y. Luo, M. Gu, M. Park, X. Fang, Y. Kwon, J. M. Urueña, J. Read de Alaniz, M. E. Helgeson, C. M. Marchetti, and M. T. Valentine, Molecular-scale substrate anisotropy, crowding and division drive collective behaviours in cell monolayers, J. R. Soc. Interface **20**, 20230160 (2023).
[63] M. F. Staddon, E. M. Munro, and S. Banerjee, Pulsatile contractions and pattern formation in excitable actomyosin cortex, PLoS Comput. Biol. **18**, e1009981 (2022).
[64] M. Besse, H. Chaté, and A. Solon, Metastability of constant-density flocks, Phys. Rev. Lett. **129**, 268003 (2022).
[65] X. Cheng and J. E. Ferrell, Jr., Spontaneous emergence of cell-like organization in *Xenopus* egg extracts, Science **366**, 631 (2019).
[66] M. Rinaldin, A. Kickuth, A. Lamson, B. Dalton, Y. Xu, P. Mejstřík, S. Di Talia, and J. Brugués, Robust cytoplasmic partitioning by solving a cytoskeletal instability, Nature (London) **651**, 501 (2026).
[67] T. J. Mitchison and C. M. Field, Self-organization of cellular units, Annu. Rev. Cell Dev. Biol. **37**, 23 (2021).
[68] M. James, D. A. Suchla, J. Dunkel, and M. Wilczek, Emergence and melting of active vortex crystals, Nat. Commun. **12**, 5630 (2021).
[69] D. J. G. Pearce, J. Nambisan, P. W. Ellis, A. Fernandez-Nieves, and L. Giomi, Orientational correlations in active and passive nematic defects, Phys. Rev. Lett. **127**, 197801 (2021).
[70] R. R. Keogh, S. Chandragiri, B. Loewe, T. Ala-Nissila, S. P. Thampi, and T. N. Shendruk, Helical flow states in active nematics, Phys. Rev. E **106**, L012602 (2022).
[71] F. Caballero, Z. You, and M. C. Marchetti, Vorticity phase separation and defect lattices in the isotropic phase of active liquid crystals, Soft Matter **19**, 7828 (2023).
[72] W. Mirza, M. De Corato, M. Pensalfini, G. Vilanova, A. Torres-Sánchez, and M. Arroyo, Theory of active self-organization of dense nematic structures in the actin cytoskeleton, eLife **13**, RP93097 (2025).
[73] J. S. Bois, F. Jülicher, and S. W. Grill, Pattern formation in active fluids, Phys. Rev. Lett. **106**, 028103 (2011).
[74] K. Vijay Kumar, J. S. Bois, F. Jülicher, and S. W. Grill, Pulsatory patterns in active fluids, Phys. Rev. Lett. **112**, 208101 (2014).
[75] L. Barberi and K. Kruse, Localized states in active fluids, Phys. Rev. Lett. **131**, 238401 (2023).
[76] L. Barberi and K. Kruse, Localized spatiotemporal dynamics in active fluids, Phys. Rev. E **110**, 054409 (2024).
[77] A. Michaud, M. Leda, Z. T. Swider, S. Kim, J. He, J. Landino, J. R. Valley, J. Huisken, A. B. Goryachev, G. von Dassow, and W. M. Bement, A versatile cortical pattern-forming circuit based on Rho, F-actin, Ect2, and RGA-3/4, J. Cell Biol. **221**, e202203017 (2022).
[78] R. Berthoz, H. Li, M. André, M. Lieb, L. Hinderling, B. Grädel, J. Van Unen, O. Pertz, K. Kruse, and D. Riveline, Interplay between Rac1/RhoA and actin waves in giant epithelial cells: Experiment and theory, Biophys. J. **125**, 3074 (2026).
[79] L. Castor, Control of division by cell contact and serum concentration in cultures of 3T3 cells, Exp. Cell Res. **68**, 17 (1971).
[80] A. Puliafito, L. Hufnagel, P. Neveu, S. Streichan, A. Sigal, D. K. Fygenson, and B. I. Shraiman, Collective and single cell behavior in epithelial contact inhibition, Proc. Natl. Acad. Sci. USA **109**, 739 (2012).
[81] M. Delarue, F. Montel, D. Vignjevic, J. Prost, J.-F. Joanny, and G. Cappello, Compressive stress inhibits proliferation in tumor spheroids through a volume limitation, Biophys. J. **107**, 1821 (2014).
[82] V. K. Gupta and O. Chaudhuri, Mechanical regulation of cell-cycle progression and division, Trends Cell Biol. **32**, 773 (2022).
[83] J. Plastino, I. Lelidis, J. Prost, and C. Sykes, The effect of diffusion, depolymerization and nucleation promoting factors on actin gel growth, Eur. Biophys. J. **33**, 310 (2004).
[84] P. Bieling, S. D. Hansen, O. Akin, T. Li, C. C. Hayden, D. A. Fletcher, and R. D. Mullins, WH2 and proline–rich domains of WASP–family proteins collaborate to accelerate actin filament elongation, EMBO J **37**, 102 (2018).
[85] C. Blanch-Mercader and J. Casademunt, Spontaneous motility of actin lamellar fragments, Phys. Rev. Lett. **110**, 078102 (2013).
[86] D. Shao, W.-J. Rappel, and H. Levine, Computational model for cell morphodynamics, Phys. Rev. Lett. **105**, 108104 (2010).
[87] F. Ziebert, S. Swaminathan, and I. S. Aranson, Model for self-polarization and motility of keratocyte fragments, J. R. Soc. Interface **9**, 1084 (2012).